Measurement 211 (2023) 112666

Contents lists available at ScienceDirect

Measurement

journal homepage: www.elsevier.com/locate/measurement

# Minimising the number of ranging sensors verifying target positioning uncertainty

Farhad Shamsfakhr [a], Luigi Palopoli [b], Daniele Fontanelli [a,*]

[a] Department of Industrial Engineering, Via Sommarive 9, 38123, Trento, Italy
[b] Department of Information Engineering and Computer Science, Via Sommarive 9, 38123, Trento, Italy

ARTICLE INFO

*Keywords:*
Optimal sensor placement
Ranging-based positioning
Uncertainty analysis

ABSTRACT

Indoor positioning applications are increasingly popular due to the availability of effective and low cost ranging sensors. Many solutions have been proposed recently using these type of sensors to estimate the coordinates (position) of a target within a given target uncertainty. In this paper, we consider the problem of deploying a large scale infrastructure that solves the positioning task with guaranteed estimation uncertainty while minimising the number of ranging sensors. To this end, we adopt a two steps procedure. In the first step, we identify a basic cell structure compounded of a small number of sensors deployed in symmetric configurations. We study the problem in general terms and we specifically focus on how to maximise the area covered by this basic structure using the smallest possible number of three ranging sensors. In the second step, we use this basic cell as an elementary tile structure to be used in standard coverage algorithm minimising the portion of space left uncovered. The approach is validated through a large number of simulations and experimental results.

## 1. Introduction

Given an entity (e.g., a person, a robot or a valuable asset of any kind) and given an environment, the positioning problem is about the use of some external measurements to find its cartesian coordinates at a given time, whereas the localisation problem is about using external measurements and ego-motion information to reconstruct its pose (cartesian coordinates + orientation) and to track it over time [1]. Both problems are instrumental to a large class of important industrial applications, and their solution is particularly difficult in the environments where the satellite-based positioning systems are not available or reliable.

The increasing availability of low cost accurate sensors has democratised the positioning and localisation technology disclosing important opportunities for its penetration in large indoor environments, once believed the most impervious to its application. An important example of this innovative type of sensors are the Ultra-Wide-Band (UWB) communication modules. An UWB node can generate a very narrow impulse that is robust to multipath fading and interference. Therefore, it is possible to set up a measurement system based on time-of-arrival (ToA) information and producing ranging measurement with an accuracy of a few centimetres. Even if this new type of sensors have made accurate positioning affordable, they require to set up an maintain an important infrastructure. This leads us to the sensor placement problem: finding a deployment that guarantees an assigned maximum target uncertainty and that requires the least number of sensors. As we will discuss in the paper, the problem is known to be NP-Hard, and in order for a solution to scale to environments of realistic size, it has to be necessarily sub-optimal. With these considerations in mind, the relevance of a solution for optimal sensor placement has to be evaluated on its ability to meet a number of practical requirements such as: **R1.** producing solutions for large environments in an acceptable time (scalability), **R2.** working with environments of arbitrary shape (generality), **R3.** keeping the number of deployed sensors close to the minimal and anyway very small (efficiency), **R4.** guaranteeing specified levels of uncertainty by countering all possible effects (e.g., of geometric nature) that could amplify the positioning error (reliability), **R5.** it has to consider physical limitations of the sensors (sensor limitations). As regards, the last requirement, we should observe that the ranging uncertainty is a function of the distance between the source and the emitter. For example, light based (e.g., LiDAR) or acoustic (e.g., Sonars) ranging systems are naturally limited by the maximum sensing distance [2]. Typical RF ranging systems suffer the same limitations. This has been observed for RSSI signals [3] but also for the ToA based measurements of UWB nodes, both in Line of Sight (LoS) [4] and in non-LoS [5] conditions.

**Related Work.** The sensor placement problem has been widely investigated in the past for different types of sensors. For example, [6]

* Corresponding author.
*E-mail addresses:* farhad.shamsfakhr@unitn.it (F. Shamsfakhr), luigi.palopoli@unitn.it (L. Palopoli), daniele.fontanelli@unitn.it (D. Fontanelli).

https://doi.org/10.1016/j.measurement.2023.112666
Received 15 October 2022; Received in revised form 23 February 2023; Accepted 26 February 2023
Available online 2 March 2023

proposed a visual landmark placement algorithm in order to meet a desired target uncertainty. This solution considers the existence of a fixed pattern, equilateral triangles with landmarks on the vertices, that has been shown to be optimal to reach the minimum uncertainty [7].

Redondi et al. [8] presented Tabu Search heuristic algorithm for finding the optimal deployment pattern of sensor nodes for an indoor localisation system based on Received Signal Strength (RSS). The approach considers a fixed number of sensors and uses the Cramer Rao Lower Bound (CRLB) as the optimality index to minimise the overall localisation error. In the same line, other papers [9,10] address the range sensors placement problems, with the mean-square localisation error being used as the optimisation index. The proposed solutions provide near-optimal deployment patterns on a free plane without considering the physical constraints of the environment. Besides, the authors do not offer any clue on the actual computational costs of the optimisation algorithm. With respect to these papers, our problem is somewhat dual: rather than minimising the uncertainty given the number of nodes, we look for the minimal number of nodes guaranteeing a target uncertainty and then build the deployment on it.

Chepuri et al. [11] proposes a solution for selecting the optimal deployment pattern of UWB nodes. The problem is modelled as the design of a sparse selection vector and its solution is based on the random selection of a sub-set of sensors which are randomly located on a well-shaped grid structure. Hence, its application cannot be generalised to environments of generic shape.

Information-theoretic-based approaches [12,13] are popular methods for optimal sensor placements, suitable for selection of heterogeneous sensors used for both observation and actuations. In [14], a sensor selection strategy for target localisation based on the maximum likelihood estimator is presented. The algorithm chooses the sensor observation that reduces the most the entropy on the target location, taking into account the prior target position pdf. The selection procedure is performed iteratively using a heuristic algorithm selecting one sensor per step. [15] investigates a unique scalar measure for the spread of the uncertainty in the structural parameter values using the Fisher information matrix. By developing a relationship between measurement redundancy and information entropy, the optimal set of sensor configurations that minimises the entropy measure is obtained. The approach has a strong relationship with the determinant of the inverse of Fisher information matrix, which encompasses the information about the values of the structural model parameters based on the data from all measured positions. Another approach based on [15] takes the knowledge of the prior distribution into account within a Bayesian framework for the placement of multi-type sensors (measurement and system actuation) of a dynamical system [16]. Here a heuristic sequential method was used for selecting the optimal locations of different types of sensors based on the overall Information Entropy. The downside of the aforementioned entropy-based methodologies is a very high computational cost to solve the discrete optimisation and obtain good estimates of sensor configurations that correspond to information entropy values close to the minimum information entropy.

The idea of seeking the optimal deployment of range sensors within fixed patterns is explored by several authors. In a number of different proposals [6,17–19], the approach is to first fix a grid of "candidate" positions for the sensors, and then apply non-convex optimisation to find the optimal deployment of sensors limiting the search to the grid. As observed by Chepuri et al. [17], the performance of an algorithm of this kind is strongly related to the choice of the search grid. A coarse grained grid may prevent the algorithm form a deployment guaranteeing the required target uncertainty, while a small grid size may easily make the problem intractable.

As a final and additional important point, none of the papers cited above dealing with ranging sensors considers the point that we have generally defined as sensor limitations (i.e., the limited sensing range). We would like also to remark that, in spite of the rich literature on the topic and of the constant reduction of the hardware costs over the past years, the sensor deployment problem remains a very active research area. Much of the scientific interest lies in the difficulty of achieving scalable solutions, of deploying anchors to difficult-to reach locations, of keeping in check the maintenance cost of the system, and of managing the communication protocol between the anchors and with the target.

**Paper Contribution.** In this paper, we propose a sensor placement solution respecting the five requirements stated above. Our solution builds on a key observation from Chen et al. [20]: an optimal ranging sensor deployment follows exact symmetrical patterns. For example, the optimal pattern for the three sensors case is an equilateral triangle, for four is a square, for six is given by two nested equilateral triangles (one triangle inside the other), etc. This observation leads us to search for the optimal symmetric configuration of a set of $n$ ranging sensors (henceforth referred to as *anchors*) that covers a region $\mathcal{P}_n$ respecting some constraints. The constraints are for us of two types: 1. each point in the region must fall within the sensing range (which is set to a finite and known value $r$) of an adequate number of anchors, 2. the positioning uncertainty within this area should be less than the desired target uncertainty. Notice that by "optimal" we mean the configuration that respects the constraints with the minimal number of anchors. Once this region has been identified and characterised, it can be used as a basic "tile" in a geometric covering algorithm [21]. Our first contribution is a characterisation of the geometric properties of the region $\mathcal{P}_n$ and an algorithm that solves the optimisation problem.

The minimal number of anchors that solve the problem is $n = 3$. However, we show as our second, and probably most important, contribution that the minimal "tile" that we should consider is not necessarily $\mathcal{P}_3$, but it is possible to find a region $\mathcal{P}_2$ with larger coverage and with the same positioning uncertainty. The validity of the approach is shown by a large number of simulations and experimental evidence.

The paper is organised as follows. In Section 2, we offer a quick overview of the main previous results and ideas the paper builds on. In Section 3, we provide a geometric characterisation of the region $\mathcal{P}_n$ and we describe an algorithm to optimise the anchor configuration to cover $\mathcal{P}_n$ with guaranteed positioning performance and minimising the number of anchors. In Section 4, we focus our attention on the case of the cell covered with the minimum possible number of anchors ($n = 3$). In particular, we show that, for every $\mathcal{P}_3$ configuration, we can find an equivalent $\mathcal{P}_2$ with the same maximum uncertainty and with a larger coverage. The approach is validated through simulation data in Section 5 and through experiments in Section 6. Finally, in Section 7, we state our conclusions and announce future work directions.

## 2. Background material

We consider the problem of estimating the position of a target within an indoor environment. To this end, we will use ranging sensors that, in the ideal case, produce a measurement modelled by the measurement function:

$$\ell_i = h_i(\mathbf{p}) = \sqrt{(X_i - x)^2 + (Y_i - y)^2}, \tag{1}$$

with $\mathbf{a}_i = [X_i, Y_i]^T$ being the Cartesian coordinates of the $i$th anchor and with $\mathbf{p} = [x, y]^T \in \mathcal{P}$ being the coordinates of the target position to be estimated. The results presented below are totally agnostic both to the choice of the sensor module (e.g., based on radio frequency, ultrasonic or light signals) and to the measurement technique (e.g., measuring the radio signal strength, the echo, the time-stamped values).

Estimating the coordinates of a target $\mathbf{p}$ at a given time by using the ranging measurements is known as a positioning problem, and its solution requires at least $n \geq 3$ measurements from non-collinear anchors [22]. On the contrary, if the target moves with known dynamics a localisation problem is adopted, whose solution leverages the motion information as well; therefore, under minimal assumptions, the minimum number of anchors required reduces to $n = 2$ [23]. In

this paper, we will restrict the focus to the positioning problem. We will make the realistic assumptions that measurements are affected by noise, and therefore the estimated position will be uncertain. We remark that the uncertainty on the position is amplified when it is used to reconstruct the pose for dynamic targets [1,24], thus making the discussion below relevant also for the localisation problem.

Because of the noise, the measurement function (1) takes the more realistic form:

$$\bar{\ell}_i = h_i(\mathbf{p}) + \eta_i = \ell_i + \eta_i. \tag{2}$$

We will assume that the uncertainties $\eta_i$ are zero mean and uncorrelated. Hence, using the expected operator $\mathrm{E}\{\cdot\}$, we have $\mathrm{E}\{\eta_i \eta_j\} = 0$ if $i \neq j$ and $\mathrm{E}\{\eta_i^2\} = \sigma_i^2$, which can be expressed more compactly with the vectorial form $\boldsymbol{\eta} = [\eta_1, \dots, \eta_n]^T$, i.e., $\boldsymbol{\Sigma}_{\boldsymbol{\eta}} = \mathrm{E}\{\boldsymbol{\eta}\boldsymbol{\eta}^T\} = \mathrm{diag}(\sigma_1^2, \dots, \sigma_n^2)$. Since (1) is nonlinear, the problem of finding a suitable estimate $\hat{\mathbf{p}}$ of $\mathbf{p}$ can be effectively solved using the following Nonlinear Weighted Least Squares (NWLS) problem

$$\hat{\mathbf{p}} = \arg\min_{\mathbf{p}} \sum_{i=1}^{n} \frac{\left(\bar{\ell} - h_i(\mathbf{p})\right)^2}{\sigma_i^2}. \tag{3}$$

An effective solution is given by the iterative Gauss–Newton solution, which, solves a point-wise linearised WLS problem

$$\overline{\boldsymbol{\ell}} \approx H_k \hat{\mathbf{p}}_{k+1} + \boldsymbol{\eta} \Rightarrow \hat{\mathbf{p}}_{k+1} = (H_k^T \boldsymbol{\Sigma}_{\boldsymbol{\eta}}^{-1} H_k)^{-1} H_k^T \boldsymbol{\Sigma}_{\boldsymbol{\eta}}^{-1} \overline{\boldsymbol{\ell}} = H_k^{\dagger} \overline{\boldsymbol{\ell}}, \tag{4}$$

where $\overline{\boldsymbol{\ell}} = [\bar{\ell}_1, \dots, \bar{\ell}_n]^T$ is the vector of measurements (2),

$$H_k = \frac{\partial h}{\partial \hat{\mathbf{p}}_k} \begin{bmatrix} \lambda_{x_1}(\hat{\mathbf{p}}_k) & \lambda_{y_1}(\hat{\mathbf{p}}_k) \\ \lambda_{x_2}(\hat{\mathbf{p}}_k) & \lambda_{y_2}(\hat{\mathbf{p}}_k) \\ \vdots & \\ \lambda_{x_n}(\hat{\mathbf{p}}_k) & \lambda_{y_n}(\hat{\mathbf{p}}_k) \end{bmatrix}, \tag{5}$$

is the Jacobian of the measurement vector $h(\mathbf{p})$, $\lambda_{x_i}(\hat{\mathbf{p}}_k) = \frac{\hat{x}_k - X_i}{\hat{\ell}_{i,k}}$, $\lambda_{y_i}(\hat{\mathbf{p}}_k) = \frac{\hat{y}_k - Y_i}{\hat{\ell}_{i,k}}$, and $\hat{\ell}_{i,k} = \sqrt{(\hat{x}_k - X_i)^2 + (\hat{y}_k - Y_i)^2}$. In this expression, $\hat{\mathbf{p}}_k$ is the estimate of $\mathbf{p}$ at the $k$th iteration of the NWLS, and is used to derive the updated estimates $\hat{\mathbf{p}}_{k+1}$. The standard approach mandates to iterate the gradient descent steps up until $\|\hat{\mathbf{p}}_{k+1} - \hat{\mathbf{p}}_k\| \leq e_{\mathbf{p}}$, where $e_{\mathbf{p}}$ is a user defined accuracy threshold. However, by exploiting geometric properties, it os possible to find an alternative technique, known as the G-WLS [25], which requires only two WLS iterations to reach the optimal theoretical bound in standard operative conditions. The first step is the solution of a linearised multilateration problem using a standard WLS, while the second step corrects the result by injecting the information on anchor geometry captured by the Geometric Dilution of Precision (GDoP) for positioning problems [26]. The two-steps algorithm leads to a position estimation error $\tilde{\mathbf{p}} = \mathbf{p} - \hat{\mathbf{p}}$ with an uncertainty given by

$$\overline{\boldsymbol{\Sigma}}_{\tilde{\mathbf{p}}_k} = (H_k^T \mathrm{E}\left\{\overline{\boldsymbol{\ell}}\overline{\boldsymbol{\ell}}^T\right\}^{-1} H_k)^{-1} = (H_k^T \boldsymbol{\Sigma}_{\boldsymbol{\eta}}^{-1} H_k)^{-1}.$$

As reported in [25], in the case of zero-mean and Gaussian uncertainties $\boldsymbol{\eta} = [\eta_1, \dots, \eta_n]^T$, the solution of the two-step G-WLS almost surely reaches the CRLB [27]

$$C(\mathbf{p}) = \left(H^T \boldsymbol{\Sigma}_{\boldsymbol{\eta}}^{-1} H\right)^{-1}, \tag{6}$$

where $H$ is the value of (5) evaluated in the actual position $\mathbf{p}$. The CRLB is a measure of the minimum theoretical estimation uncertainties achievable by an estimator, hence this certifies the effectiveness of the two steps approach.

Moreover, in the assumption of homoscedasticity of the ranging uncertainties, i.e., $\boldsymbol{\Sigma}_{\boldsymbol{\eta}} = \sigma_{\ell}^T I_m$, we have

$$\overline{\boldsymbol{\Sigma}}_{\tilde{\mathbf{p}}_k} = \sigma_{\ell}^2 (H_k^T H_k)^{-1}. \tag{7}$$

This quantity is tightly related to the GDoP $g(\mathbf{p})$ [28,29]:

$$g(\mathbf{p}) = \sqrt{\mathrm{Tr}\left((H_k^T H_k)^{-1}\right)} = \frac{\sqrt{\mathrm{Tr}\left(\overline{\boldsymbol{\Sigma}}_{\tilde{\mathbf{p}}_k}\right)}}{\sigma_{\ell}}, \tag{8}$$

where $\mathrm{Tr}(\cdot)$ is the trace of a matrix and $\tilde{\mathbf{p}}_k = \mathbf{p} - \hat{\mathbf{p}}_k$. The lower is the GDoP, the lower is the uncertainty on $\tilde{\mathbf{p}}_k$, since $(H_k^T H_k)^{-1}$ acts as a multidimensional gain for the ranging uncertainties.

### 2.1. Problem formulation

Since the CRLB (6) can be attained using the G-WLS [25] and it is intrinsically related to the GDoP (8), we will consider the GDoP as the cost index to guide the optimal deployment of the ranging sensors. In particular, given the set of all the feasible positions $\mathcal{P}$, we want to minimise the number $n$ of ranging anchors deployed in the environment in order to have $g(\mathbf{p}) \leq g^{\star}$, $\forall \mathbf{p} \in \mathcal{P}$, where $g^{\star}$ is the maximum desired value for the GDoP. We will explicitly consider *limited sensing range* $r$ for the anchors, which will be modelled by setting $\bar{\ell}_i = -1$ in (2) if $\ell_i > r$ in (1) (e.g., no echo is detected in Time-of-Flight ranging sensors).

## 3. Geometric analysis

One common approach to ranging anchors deployment is to first grid the space $\mathcal{P}$ with a sequence of $m$ points on a grid, displaced at distance $d$. Next, by regularly sampling $\mathbf{p}_h \in \mathcal{P}$, $h = 1, \dots, q$, it is possible to compute the gradients $H_{i,h}$ (the rows of (5)) for the $i$th grid position, $i = 1, \dots, m$, in the $h$th sampled position $\mathbf{p}_h$, $h = 1, \dots, q$. Assuming homoscedasticity for the uncertainties and using the selection vector $\mathbf{w} = [w_1, w_2, \dots w_m]^T \in \{0,1\}^m$, where $w_i = 1$ if the sensor is placed in the $i$th position or zero otherwise, it is possible to set the following optimisation problem [17]

$$\min_{\mathbf{w} \in \{0,1\}^m} \|\mathbf{w}\|_0 \text{ s.t. } \sigma_{\ell}^2 \mathrm{Tr}\left(\left(\sum_{i=1}^{m} w_i H_{i,h}^T H_{i,h}\right)^{-1}\right) \leq \lambda, \forall h \tag{9}$$

where the $\|\mathbf{w}\|_0$ is a quasi norm counting the number of non-zero entries of $\mathbf{w}$ and $\lambda$ is the desired target uncertainty for the position estimates. Since

$$\mathrm{Tr}\left(\left(\sum_{i=1}^{m} w_i H_{i,h}^T H_{i,h}\right)^{-1}\right) = \mathrm{Tr}\left(\left(H_h^T H_h\right)^{-1}\right),$$

where $H_h$ is the Jacobian (5) evaluated in position $\mathbf{p}_h$ and for the anchors in grid position $i$ where $w_i = 1$, the minimisation problem (9) is substantially equivalent to the GDoP uncertainty gain minimisation in (8) and this further corroborates our choice of the GDoP as a cost function. With this approach, the performance very much depends on the grid's choice [17], and it is not possible to consider a limited sensing range.

To overcome these important limitations, we will consider an approach in which the search for the optimal configuration is made in a continuous space. Our idea to reduce the complexity is based on two steps. In the first step, we identify a basic "tile" $\mathcal{P}_n \subseteq \mathcal{P}$, in which $n$ anchors are optimally deployed so that the GDoP constraint is satisfied, i.e. $g_n(\mathbf{p}) \leq g^{\star}$, $\forall \mathbf{p} \in \mathcal{P}_n$. This search is simplified by two facts: 1. the optimal solution can be sought between the symmetric configurations of the anchors [20], 2. the behaviour of the GDoP is monotone in the number of anchors $g_n(\mathbf{p}) \geq g_{n+1}(\mathbf{p})$ (i.e., given a configuration with $n$ anchors, randomly adding an anchor will never increase the GDoP). The second fact has an additional benefit: if we consider two tiles $\mathcal{P}_n$, any point $\mathbf{p}$ in the overlapping region will respect $g(\mathbf{p}) \leq g^{\star}$. This leads us to the second step: once the basic tile $\mathcal{P}_n$ structure is defined, it can be replicated to cover the entire space using standard tile coverage algorithms (see Section 5.1).

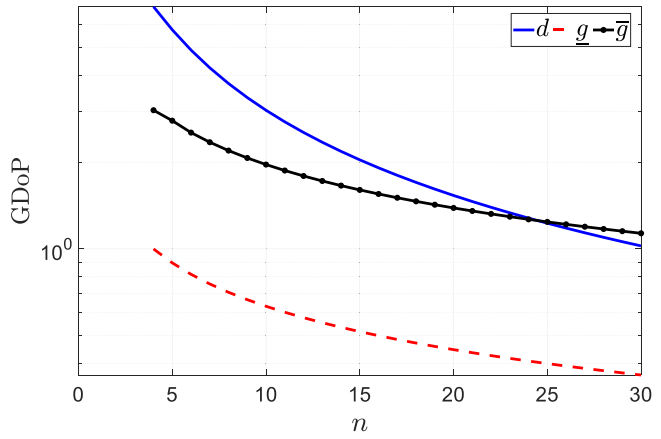


**Fig. 1.** Behaviour of $d$ (solid), $\underline{g}$ (dashed) and $\overline{g}$ as a function of the number of anchors and with a fixed radius $\delta$.

### 3.1. $\mathcal{P}_n$ region

In this first part of the discussion, we characterise the most important properties of the region $\mathcal{P}_n$. As reported in [20], given a set of $n \geq 3$ anchors the most convenient configuration for GDoP minimisation is one in which the anchors are optimally deployed on a circle. Indeed, the matrix $H_k$ in (5) can be expressed as (the subscript $k$ in (4) is not needed in this context)

$$H = \begin{bmatrix} \cos(\gamma_1) & \sin(\gamma_1) \\ \cos(\gamma_2) & \sin(\gamma_2) \\ \vdots & \\ \cos(\gamma_n) & \sin(\gamma_n) \end{bmatrix},$$

where $\gamma_i = \arctan\frac{y-Y_i}{x-X_i}$, with the evaluation point $\mathbf{p} = [x, y]^T$ and the anchor position $\mathbf{a}_i = [X_i, Y_i]^T$, which leads to [25]

$$g_n(\mathbf{p}) = \sqrt{\frac{n}{\sum_{i=1}^{n-1}\sum_{j=i+1}^{n}\sin(\gamma_j - \gamma_i)^2}} = \sqrt{\frac{n}{D_n}}. \tag{10}$$

Three important propositions are now stated.

**Proposition 1.** *Within the $\mathcal{P}_n$ region, the GDoP $g_n(\mathbf{p})$ is non-increasing with $n$. As an example, in Fig. 1, shows the lower bound $\underline{g} = \min_{\mathbf{p}} g_n(\mathbf{p})$ with a dashed line and the upper bound $\overline{g} = \max_{\mathbf{p}} g_n(\mathbf{p})$ with a dotted line. As it is possible to see both decrease with $n$.*

**Proposition 2.** *If we neglect such adverse effects as reflections or multipath (as we do in this context to keep our discussion neutral with respect to the adopted technology), the inspection of (10) and the results shown in [25] reveal that the optimal deployment is simply given by a symmetric configuration with a distance $d$ among the anchors.*

**Proposition 3.** *Considering again Eq. (10), for a symmetric configuration of the anchors, the lowest GDoP is attained at the centre of the anchors configuration, i.e., $\underline{g} = g_n(\mathbf{p}_c)$.*

Given the centre $\mathbf{p}_c = [x_c, y_c]^T$ of the circle of radius $\delta$ upon which the anchors are deployed, in view of Proposition 2, the anchors will be deployed in the following position

$$\mathbf{a}_i = p_c + \delta[\cos\theta_i, \sin\theta_i]^T, \tag{11}$$

where $\theta_i = 2i\pi/n$, $i = 1, \ldots, n$, with the Euclidean distance between two adjacent anchors expressed using the 2-norm $\|.\|$ being

$$d = 2\delta\sin(\pi/n) = \|\mathbf{a}_i - \mathbf{a}_{i+1}\|, \forall i \in \{1, \ldots, n\}, \tag{12}$$

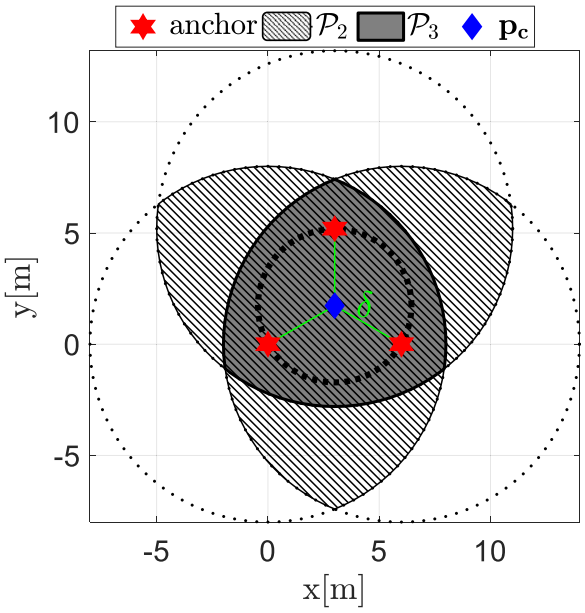


**Fig. 2.** $\mathcal{P}_3$ region (solid fill) and $\mathcal{P}_2$ region (line pattern fill) with $r = 8$ [m] and $d = 0.75r$.

with the implicit assumption that $\mathbf{a}_{i+1} = \mathbf{a}_1$ for the periodicity of the circular deployment. Increasing the number $n$ of anchors, will reduce their mutual distance $d$ (solid blue line in Fig. 1), and will reduce the GDoP (Proposition 1). Finally, the minimum GDoP will be attained in $\mathbf{p}_c$ (Proposition 3).

By making the choice in (11) and considering a limited sensing range $r$, we can choose $\mathcal{P}_n$ as a symmetric region having the same centre $\mathbf{p}_c$ as the anchor configuration. If we account for the limited sensing range, the area has to fall within the intersection of the circles centred in the anchors with radius $r$. As a result $\mathcal{P}_n$ can be defined as

$$\mathcal{P}_n = \left\{\mathbf{p} \in \mathcal{P} | h_i(\mathbf{p}) \leq r \ \forall i \in \{1, \ldots, n\} \wedge g_n(\mathbf{p}) \leq g^\star\right\}, \tag{13}$$

where $n \geq 3$.

We can now formulate a few constraints stemming from purely geometric considerations.

- If $\delta > r$, it follows that $\mathbf{p}_c \notin \mathcal{P}_n$, which means that $\mathbf{p}_c$ should be covered by additional anchors, hence a minimal deployment cannot be reached. If $\delta = r$ and $g_n(\mathbf{p}_c) \leq g^\star$, we have $\mathbf{p}_c \equiv \mathcal{P}_n$, which is of course a non minimal configuration. Therefore, we will assume that $\delta < r$.
- If $\delta < r$ and $g_n(\mathbf{p}_c) > g^\star$, in view of Proposition 3, we have $\mathcal{P}_n = \emptyset$. In this case, it is possible just to increase the number of anchors $n$ deployed on the circle of radius $\delta$ up until we reach the condition $\mathcal{P}_n \neq \emptyset$. The GDoP equation (10) proves that this condition is achieved for a sufficiently large number of anchors (see Fig. 1).
- Given $\delta < r$ and $g_n(\mathbf{p}_c) \leq g^\star$, we have from (12) that $d < 2r$. The situation is the one displayed in Fig. 2 for an example with $n = 3$.

Notice that since the GDoP depends only on the geometry of the deployment, the value of the minimum GDoP $g_n(\mathbf{p}_c)$ for a fixed $n$ does not change $\forall\delta > 0$. However, the region covered respecting the constraint $g_n(\mathbf{p}) \leq g^\star$ shrinks when $\delta$ decreases due to (10). On the other hand, since $\mathcal{P}_n$ in (13) has to fall within the sensing range of all anchors, its maximum extension is given by the intersection of the $n$ circles centred in the anchors, i.e., constrained by $r$ (see the dark-solid shaded area in Fig. 2). AS a consequence, the area jointly covered by the anchors shrinks when the anchors are pushed farther away by

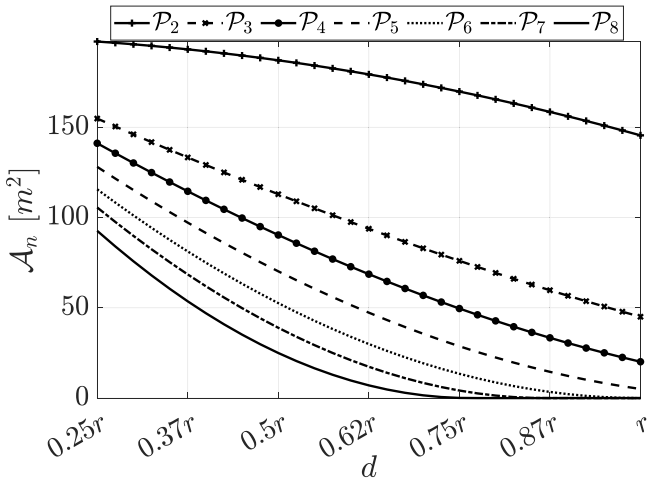


**Fig. 3.** The coverage area for different number of anchors.

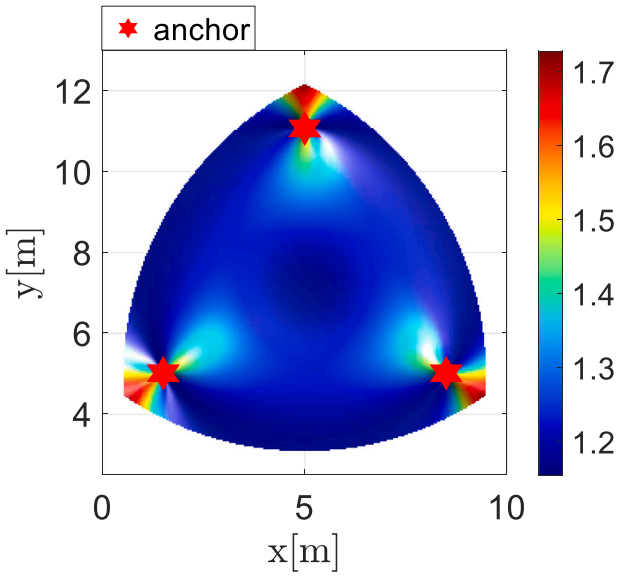


**Fig. 4.** GDoP $g_3(\mathbf{p})$ surface with colour scale for $\mathcal{P}_3$ when $r = 8$ [m] and $d = 0.87r$.

increasing $\delta$, thus the anchors will be pushed outside the region $\mathcal{P}_n$. This is clearly visible in Fig. 3 where we report

$$\mathcal{A}_n = \int_{\mathbf{p}\in\mathcal{P}_n} \mathbf{p}\, d\mathbf{p}, \tag{14}$$

as a function of the distance $d$ for fixed $r$; However, since we are looking for the tile configuration that facilitates the coverage of the entire work-space by means of a set of overlapping tiles, it is convenient to consider configurations for which the anchors fall within $\mathcal{P}_n$, which implies $d < r$. By using (12), this choice implies:

$$\delta \leq \frac{r}{2\sin(\pi/n)}. \tag{15}$$

A final fact needs to be stated on the point within the region $\mathcal{P}_n$ that produces the worst (i.e., the maximum) GDoP. Assuming that the configuration is chosen so that $\mathcal{P}_n$ contains all the $n$ anchors (as per the previous observations) let

$$C(a) = \{\mathbf{p} \in \mathcal{P} | \mathbf{p} = \mathbf{p}_c + a\delta[\cos\alpha, \sin\alpha]^T, \alpha \in [0, 2\pi)\}. \tag{16}$$

For $a > 1$ this is a circular region enclosing the circle where the anchors are deployed, e.g., it encloses the thick dotted line circle of radius $\delta$ in the example of Fig. 2. By using (10), it is possible to show the following:

**Proposition 4.** *Let $C(a)$ be the region defined in (16) and let the configuration of the anchor be symmetric with respect to (15) (i.e., the anchors fall inside $\mathcal{P}_n$). Let $\mathbf{p}_M(a) = \arg\max_{\mathbf{p}\in C(a)} g_n(\mathbf{p})$, i.e. $g_n(\mathbf{p}_M(a)) = \max_{\mathbf{p}\in C(a)} g_n(\mathbf{p})$. For small enough $a$ and given (16), we have that $\mathbf{p}_M(a)$ is attained exactly by the angles*

$$\alpha \in \left\{ \arctan\left(\frac{Y_1 - y_c}{X_1 - x_c}\right), \ldots, \arctan\left(\frac{Y_n - y_c}{X_n - x_c}\right) \right\},$$

*i.e., $\mathbf{p}_M(a)$ is along the direction from the centre $\mathbf{p}_c$ to each of the anchors $\mathbf{a}_i$, $i = 1, \ldots, n$. This fact is true for any choice of $\delta$ respecting the hypotheses.*

We observe that the result of Proposition 4 is strictly true only for small $a$, since, if $a$ increases, the curves at constant GDoP tends to be circles, hence the GDoP has the same value on $C(a)$ for any angle $\alpha$. However, $\forall a > 1$ and due to the anchors symmetric configuration, we have that the following holds always true

$$\mathbf{p}_M(a) = \left\{ \mathbf{p} \in C(a) | \alpha = \arctan\left(\frac{Y_1 - y_c}{X_1 - x_c}\right) \right\}. \tag{17}$$

### 3.2. Example: $\mathcal{P}_3$ region

It is known that in order to solve the position problem with ranging measurements (2) there should be at least $n = 3$ anchors in non-collinear configuration [23]. So it is very interesting to study the shape of the $\mathcal{P}_3$ region. As shown in Fig. 2 (dark-solid shaded region), if we use exactly three ranging measurements to reconstruct the target position, $\mathcal{P}_3$ is a circular triangle. The values of $g_3(\mathbf{p})$, i.e., the GDoP for $\mathbf{p} \in \mathcal{P}_3$, is graphically depicted in Fig. 4 with a colour scale assuming $d = 0.87\ r$. The geometric position estimation uncertainty $g_3(\mathbf{p})$ increases when the target moves towards the vertexes of the circular triangle (the intersection points among the circles centred in the three anchors with radius $r$), which are the locations of $\mathbf{p}_M(a)$ given in Proposition 4.

### 3.3. Anchor deployment for $\mathcal{P}_n$ region

After characterising the most important properties of our basic "tile" $\mathcal{P}_n$, we are know in a condition to discuss Algorithm 1, which computes the optimal tile and its anchor configuration. The algorithm takes as input the centre of tile $\mathbf{p}_c$, the sensing radius $r$ and the target maximum uncertainty value expressed with the GDoP $g^\star$. It returns the minimum number of anchors needed to achieve the result and the radius $\delta$ of the circle they are to be deployed on using (11). The algorithm exploits the results on the characterisation of $\mathcal{P}_n$ for symmetric configurations discussed above. The number of anchors is initially set to $n = 3$ (the minimum value). A first do-while loop increases $n$ until the minimum value of the GDoP is less than $g^\star$, which, in view of Proposition 3, is to be found at $p_c$ independently of $n$. This loop exploits the monotonicity of GDoP with the number of anchors (Proposition 1). The second do-while loop enforces the condition $g(\mathbf{p}_M(a)) \leq g^\star$. To this end, it exploits a function $\text{find}_a$ which looks for the smallest value of the scaling factor $a > 1$ such that the maximum GDoP $g(\mathbf{p}_M(a))$ evaluated on $C(a)$ meets the constraints (see Proposition 4). If no point $\mathbf{p}_M(a)$ respecting the property exists, the loops considers a configuration with a greater number of anchors (notice that a solution surely exists by Proposition 1 and the fact that $g(\mathbf{p}_c) \leq g^\star$). After the search is completed, we have to increase the deployment radius $\delta$ until the point $\mathbf{p}_M(a)$ falls inside the sensing range of the anchors (it is worth recalling that the position of $\mathbf{p}_M(a)$ does not depend on $\delta$ by Proposition 4). To this end the algorithm finds the anchor $\bar{\mathbf{a}}$ that, in the current configuration, is the farthest from $\mathbf{p}_M(a)$. If $n$ is even there is only one $\bar{\mathbf{a}}$ and $\delta$ is given by $\frac{r}{a+1}$. If $n$ is odd, we have two anchors $\mathbf{a}_{1,2}$ at the same distance from $\mathbf{p}_M(a)$. In this case, it is sufficient to compute the base length (which is the distance $d$) of an isosceles triangle with vertices in $\mathbf{a}_1$, $\mathbf{a}_2$ and $\mathbf{p}_M(a)$, i.e., $d = r\| \frac{\mathbf{a}_1 - \mathbf{p}_M(a)}{\|\mathbf{a}_2 - \mathbf{p}_M(a)\|} - \frac{\mathbf{a}_2 - \mathbf{p}_M(a)}{\|\mathbf{a}_2 - \mathbf{p}_M(a)\|} \|$, and then compute $\delta$ reverting (12), i.e., $\delta = \frac{\|\mathbf{a}_1^\star - \mathbf{a}_2^\star\|}{2\sin(\pi/n)}$.

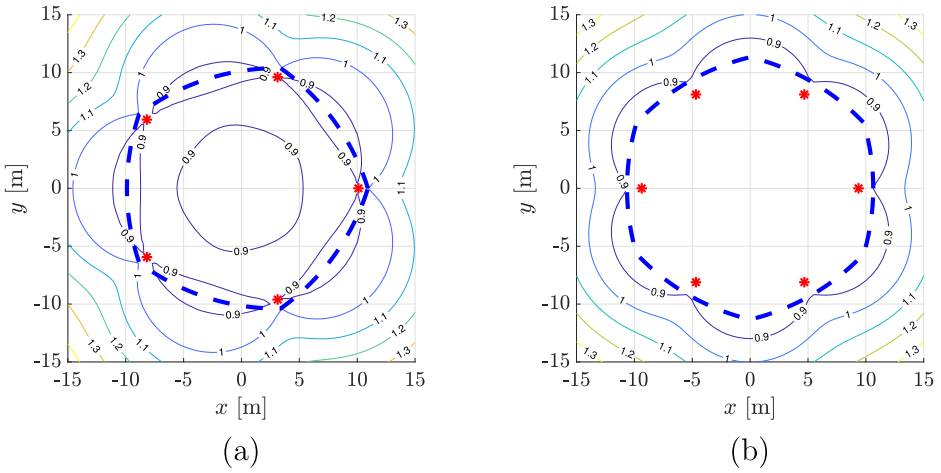


**Fig. 5.** Placement when $r = 20$ m. The thick dashed line represents the cell contour, while the GDoP contour values for $g_5(\mathbf{p})$ (a) and $g_6(\mathbf{p})$ (b) are reported accordingly. The placement for $g^\star = 1$ results in $d = 0.6r$ and $\delta = 0.5r$ (a), while for $g^\star = 0.9$ with $d = 0.55r$ and $\delta = 0.47r$ (b).

**Algorithm 1** Optimal anchor configuration

**Input:** central point $\mathbf{p}_c$, sensing radius $r$, desired $g^\star$
**Output:** deployment radius $\delta$, anchor number $n$

$n = 3$; $\delta$ =<minimum possible value>;
flag = true
**do**
  $\underline{g} = g_n(\mathbf{p}_c)$
  **if** $\underline{g} \geq g^\star$ **then** n = n + 1
  **else** flag = false
**while** flag
flag = true
**do**
  $\mathbf{a}_i = \mathbf{p}_c + \delta[\cos 2i\pi/n, \sin\cos 2i\pi/n]^T$, $i = 1 \ldots n$
  $[p_M(a), a] = \text{find}_a(g^\star)$
  **if** $p_M(a) == \emptyset$ **then** $n = n + 1$
  **else** flag = false
**while** flag
**if** $n$ is even **then**
  $\bar{\mathbf{a}} = \text{argmax}_{\mathbf{a}\in\mathbf{a}_i} |\mathbf{a} - \mathbf{p}_M(a)|$
  $\delta = r/(a+1)$
**else**
  $\bar{\mathbf{a}}_{1,2} = \text{argmax}_{\mathbf{a}\in\mathbf{a}_i} |\mathbf{a} - \mathbf{p}_M(a)|$
  $d = r\| \frac{\mathbf{a}_1 - \mathbf{p}_M(a)}{\|\mathbf{a}_1 - \mathbf{p}_M(a)\|} - \frac{\mathbf{a}_2 - \mathbf{p}_M(a)}{\|\mathbf{a}_2 - \mathbf{p}_M(a)\|} \|$; $\delta = \frac{\|\mathbf{a}_i^\star - \mathbf{a}_j^\star\|}{2\sin(\pi/n)}$
**return** $\delta$, $n$

Example of placements using the previous algorithm for $g^\star = 1$ and $g^\star = 0.9$ are reported in Fig. 5. In the first example, we have an odd number of anchors, resulting in $d = 0.59r$ and $\delta = 0.505r$, while in the second more stringent case we have an even number of anchors, resulting in $d = 0.55r$ and $\delta = 0.468r$, i.e. a more dense deployment, as consequence of the higher performance required in terms of GDoP. Notice that the results are reported as a function of $r$ since the graphs will be simply scaled for different values of $r$: Fig. 5 reports an exemplifying value of $r = 20$ m. It is worthwhile to note that the cell for $\mathcal{P}_5$ and $\mathcal{P}_6$ are intersections of circles centred in the anchors positions (thick dashed lines in Fig. 5). Finally, it is clear that with $n = 5$ we cannot ensure $g^\star = 0.9$ (see the value of the level curves of $g_5(\mathbf{p})$ in Fig. 5-a), unless a drastically reduced area (with anchors outside the deployment) is obtained. Hence, the minimum value needed is $n = 6$ (Fig. 5-b).

## 4. Beyond $\mathcal{P}_3$: the $\mathcal{P}_2$ case

The need to collect at least three anchor measurements is a geometric constraint, which is apparently impossible to surmount. The problem is very simple: if we use two anchors the point to localise can generally be in two different locations, corresponding to the intersection of two circles. This consideration leads us to define $\mathcal{P}_3$ as a subset of the intersection of the three circles within the sensing set of the three anchors. However, if we look for a coverage with minimal number of anchors that meets the target maximum uncertainty (maximum GDoP) we can work around this limitation. In the following, we first discuss how to define a basic tile out of three anchors, dubbed $\mathcal{P}_2$, that covers a larger area than $\mathcal{P}_3$ (Section 4.1). Indeed, starting from $\mathcal{P}_3$ (intersection of three circles), $\mathcal{P}_2$ is obtained by adding the areas where only two circles intersect. As will be discussed in Section 4.2, in the areas of $\mathcal{P}_2$ we can still exploit our knowledge on the anchor positions to solve the ambiguity. Importantly, we will see in Section 4.3 that by using $\mathcal{P}_2$ instead of $\mathcal{P}_3$ we can cover a larger area without sacrificing the worst case GDoP, i.e., still meeting the target maximum uncertainty requirement.

### 4.1. The $\mathcal{P}_2$ region

The region $\mathcal{P}_2$ is still defined using $n = 3$ anchors, but we release the assumption on their visibility requiring that at least three of them are simultaneously in sight. More formally, by handling (13), we have

$$\mathcal{P}_2 = \{\mathbf{p} \in \mathcal{P} | \exists i, j \in \{1,2,3\} \text{s.t.} (h_i(\mathbf{p}) \leq r \wedge h_j(\mathbf{p}) \leq r) \wedge g_2(\mathbf{p}) \leq g^\star\}.$$

The region $\mathcal{P}_2$ thus defined is exemplified in Fig. 2, where it is covered wit a linear pattern. The area covered by $\mathcal{P}_2$ is significantly larger than $\mathcal{P}_3$ (see Fig. 3 or compare Figs. 4 and 6 for the same anchor deployment). The $\mathcal{P}_2$ region forms a three lens-shaped region. As can be observed from the corresponding GDoP plot of Fig. 6, the target positioning uncertainty using two anchors increases at the circle intersections, while it reaches its highest value right behind each anchor, exactly as it happens for the $\mathcal{P}_3$ cells (recall Section 3.1).

### 4.2. Positioning with $\mathcal{P}_2$

Clearly, when a point lies at the intersection between the sensing circles of the three anchors, its position $\hat{\mathbf{p}}$ can be estimated using standard trilateration [24]. However, for the particular deployment we

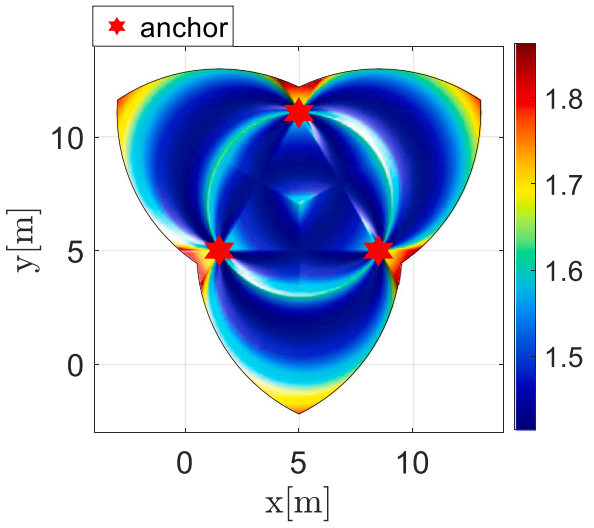


**Fig. 6.** GDoP $g_2(\mathbf{p})$ surface with colour scale for $\mathcal{P}_2$ when $r = 8$ [m] and $d = 0.87r$.

described for $\mathcal{P}_2$, $\hat{\mathbf{p}}$ can be estimated even with two anchors measurements. Considering the shaded area with line pattern fill in Fig. 2, this condition occurs in the three areas not covered by the dark grey solid fill. Importantly, in each of these three regions, the pair of anchors in view are different and this information is available. Moreover, from any pair of anchors at distance $d$, say $\mathbf{a}_i$ and $\mathbf{a}_j$, it is possible to express the position $\mathbf{p}$ in a reference frame expressed in Fig. 7 and dubbed $\mathbf{p}^\star$ using the following transformation

$$\mathbf{p}^\star = \begin{bmatrix} \cos(\phi) & \sin(\phi) \\ -\sin(\phi) & \cos(\phi) \end{bmatrix} (\mathbf{p} - \mathbf{a}_i) = R(\phi)\,(\mathbf{p} - \mathbf{a}_i)\,,$$

where $\phi = \arctan\left(\frac{Y_j - Y_i}{X_j - X_i}\right)$. With respect to this reference frame, the position $\mathbf{p}$ given two ranging measurements is given by

$$\mathbf{p}^\star = \begin{bmatrix} \frac{d^2 - \ell_j^2 - \ell_i^2}{2d} \\ \pm\sqrt{\frac{4d^2\ell_i^2 - (d^2 - \ell_j^2 + \ell_i^2)^2}{4d^2}} \end{bmatrix},$$

hence expressing the ambiguity along the $y$ direction. As a consequence,

$$\mathbf{p} = R(\phi)^T \mathbf{p}^\star + \mathbf{a}_i. \tag{18}$$

It is now evident that there are two locations for $\mathbf{p}$, which are symmetric with respect to the segment passing through $\mathbf{a}_i$ and $\mathbf{a}_j$. With respect to Fig. 2, it follows that either $\mathbf{p}$ is in the shaded dark grey area or in the line pattern fill, condition that can be easily verified by the presence or not of the third ranging measurement. As such, there is no ambiguous location for the $\mathcal{P}_2$ cell. Since the estimated location $\hat{\mathbf{p}}$ is given by the NWLS applied to the $\mathcal{P}_2$ cell, we dubbed this solution algorithm as NLS.

**Remark 1.** The possibility of resolving the ambiguity is subject to some geometric conditions. Indeed, when $d \leq r$, the ambiguous location can be always uniquely determined by the presence or absence of third anchor measurement (see Fig. 8(a)). On the other contrary, if $d > r$, it is possible to have ambiguities (see Fig. 8(b)). Notice that, as discussed in Section 3.1, the fact that the anchors fall within $\mathcal{P}_n$, implies $d < r$, hence no ambiguous locations exist.

**Remark 2.** The presence or absence of the third measurement, is instrumental to set up the NWLS in (3)–(5). Indeed, since that is a gradient descent-like algorithm, if the initial location is set at the centre of the region with line pattern fill or in the dark grey shaded area of Fig. 2, the algorithm will inevitably converge towards the correct location.

### 4.3. Positioning uncertainty in $\mathcal{P}_2$ and $\mathcal{P}_3$ cells

As discussed in Section 3 (Proposition 1) for a fixed distance $d$ between the anchors the GDoP improves with the number $n$ of anchors. Hence, $\mathcal{P}_3$ yields a smaller GDoP value than $\mathcal{P}_2$. Nonetheless, we will now show that given a generic $\mathcal{P}_3$, it is possible to define $\mathcal{P}_2$ such that $\max_{\mathbf{p}\in\mathcal{P}_2} g_2(\mathbf{p}) = \max_{\mathbf{p}\in\mathcal{P}_3} g_3(\mathbf{p})$ with a larger area covered by $\mathcal{P}_2$. However, we will have to allow for a slightly larger distance between the anchors in $\mathcal{P}_2$ than in $\mathcal{P}_3$.

**Theorem 1.** *For any $\mathcal{P}_3$ cell with $d \leq r$, there exists a $\mathcal{P}_2$ cell such that $\max_{\mathbf{p}\in\mathcal{P}_2} g_2(\mathbf{p}) = \max_{\mathbf{p}\in\mathcal{P}_3} g_3(\mathbf{p})$ as defined in (10) and having $\mathcal{A}_2 \geq \mathcal{A}_3$ as defined in (14). The distance between the anchors is $\beta d$, with*[1]*:*

$$\beta = \sqrt{\xi \pm \sqrt{\xi^2 - 2\xi + \frac{2}{3}}} \text{ and } \xi = \frac{2r^2}{d^2}. \tag{19}$$

**Proof.** Without loss of generality, let us consider the anchors are deployed as in (11) and located at

$$\mathbf{a}_1 = \begin{bmatrix} 0 \\ 0 \end{bmatrix}, \mathbf{a}_2 = \begin{bmatrix} d \\ 0 \end{bmatrix} \text{ and } \mathbf{a}_3 = \begin{bmatrix} d\cos\pi/3 \\ d\sin\pi/3 \end{bmatrix},$$

i.e., the vertices of an equilateral triangle, which is the configuration for three anchors discussed in Section 3. Consider the point corresponding to the maximum GDoP $\overline{\mathbf{p}}_{M_i} = [x, y]^T \in \mathbf{p}(a)$ defined in (17) for the $i$th cell $\mathcal{P}_i$, i.e., the locations $\overline{\mathbf{p}}_{M_2}$ and $\overline{\mathbf{p}}_{M_3}$ with maximum GDoP given by the intersection of two and three circles, respectively, of radius $r$ (see Fig. 7). Considering that the anchors for $\mathcal{P}_2$ are at distance $\beta d$, with $d$ being their distance for $\mathcal{P}_3$. We can compute the explicit GDoP in the two points applying (10):

$$\begin{aligned} g_3(\overline{\mathbf{p}}_{M_3}) &= \sqrt{\frac{3}{\sum_{i=1}^{i=2}\sum_{j=i+1}^{j=3}\sin(\gamma_i - \gamma_j)^2}} = \sqrt{\frac{3r^4}{y^2d^2 + 2r^2x^2}}, \\ g_2(\overline{\mathbf{p}}_{M_2}) &= \sqrt{\frac{2r^4}{y^2\beta^2d^2}}. \end{aligned} \tag{20}$$

By imposing $g_2(\overline{\mathbf{p}}_2) = g_3(\overline{\mathbf{p}}_3)$ and solving for $\beta$, we have the following two roots

$$\beta = \sqrt{\xi \pm \sqrt{\xi^2 - 2\xi + \frac{2}{3}}} \text{ and } \xi = \frac{2r^2}{d^2}, \tag{21}$$

yielding non-complex values for $r > 0$ and $d \leq r$, with two positive roots.

The last step to complete the proof is to show that, by setting the distance between the anchors in $\mathcal{P}_2$ to $\beta d$, we have $\mathcal{A}_2 \geq \mathcal{A}_3$. $\mathcal{A}_2$ is obviously larger than $\mathcal{A}_3$ when the anchors are deployed at the same distance (see Fig. 3). When the anchors for $\mathcal{P}_2$ are deployed at distance $\beta d$, the area covered by $\mathcal{A}_2$ decreases by increasing $\beta$. It can be seen that for any choice of $r > 0$ and $d \leq r$, we have $\mathcal{A}_2 > \mathcal{A}_3$, if $\beta \leq 1.7$ (see [30]). It can be seen that for any value of $\xi$ in (19), one of the two solutions for $\beta$ is always smaller than 1.7. Therefore, it is possible to find a region $\mathcal{A}_2$ greater than $\mathcal{A}_3$ and with equal worst case GDoP.

**Remark 3.** The cell $\mathcal{P}_2$ constructed as discussed in Theorem 1 is guaranteed to have the same worst case GDoP and a better coverage than the corresponding $\mathcal{P}_3$. The price to pay is that the GDoP (and hence the uncertainty) can be worse in the average. Indeed, the uncertainty of the estimates degrades when the target lays on the line pattern filled area of Fig. 2.

**Remark 4.** The value $\beta = 1.7$ is actually an upper bound for the "legal" ranges of $\beta$, i.e., the ones that guarantee $\mathcal{A}_2 \geq \mathcal{A}_3$. We know

[1] Albeit negative solutions for $\beta$ exists, they have no physical meaning.

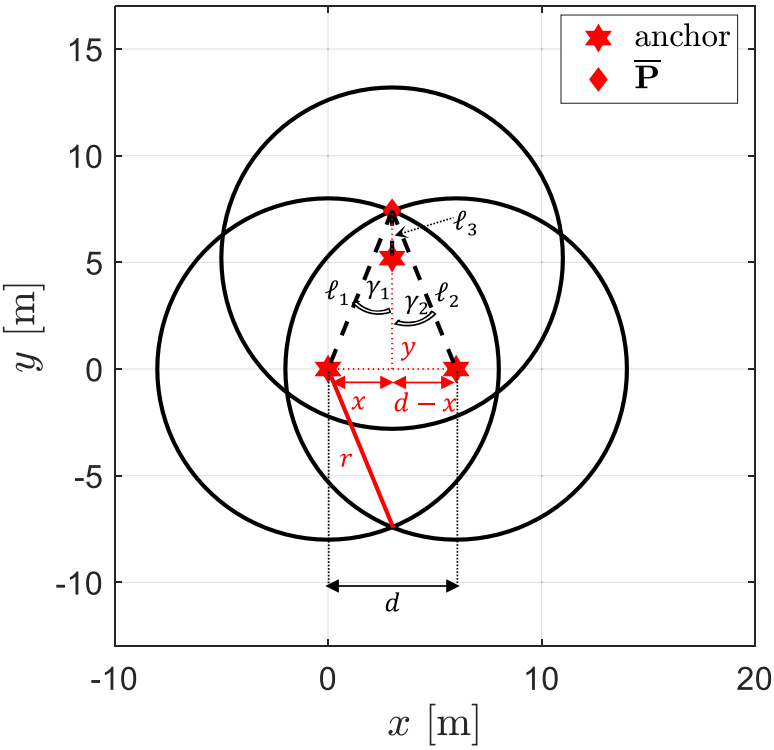


**Fig. 7.** The geometry of the worst GDOP.

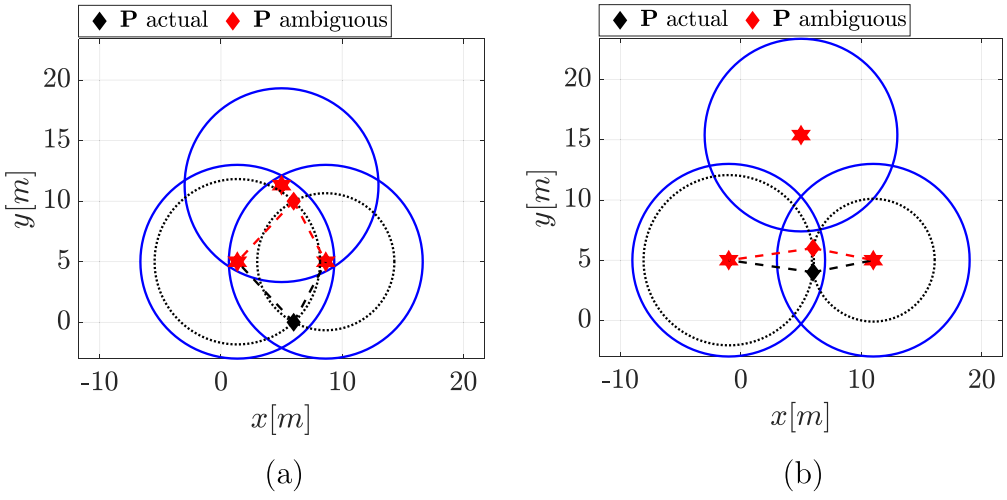


**Fig. 8.** The necessary condition for $\mathcal{P}_2$ to resolve the ambiguity in position estimation using two anchors.

that this bound is actually conservative and we are currently looking for the tightest possible bound that guarantee this geometric property. In the next section, we empirically obtain an approximate value for this bound, which we define as the "approximate optimal bound for positioning uncertainty" in $\mathcal{P}_2$.

## 5. Simulation results

As a first goal, we aimed for a numeric comparison between $\mathcal{P}_2$ and $\mathcal{P}_3$ cell geometry. The comparison was made on the efficiency gain (i.e., number of anchors needed) and on the positioning accuracy. Since an experimental comparison would have required a massive deployment of anchors, we decided to use simulation data. The reader interested in an accurate evaluation of the trilateration uncertainty adopting as ranging sensors UWB anchors is referred to our previous work [25].

We considered a simulated map generated by the Robotics System Toolbox of Matlab R2020a Software with the total coverage area of 557 $m^2$. We have considered the maximum sensing range to be $r = 8$ m and a maximum GDOP value of $g^\star = 1.98$, which resulted in an anchor distance of $d = 6$ m for the $\mathcal{P}_3$ cell. With the same constraints, the anchor distance for the $\mathcal{P}_2$ obtained with the scaling parameter $\beta$ in (19) was given by $d = 6.2$ m ($\beta = 1.03$).

For the deployment results, since we have fully characterised the regions $\mathcal{P}_j \subseteq \mathcal{P}$ so that the limited sensing range $r$ is satisfied and $g_j(\mathbf{p}) \leq g^\star$, $\forall \mathbf{p} \in \mathcal{P}_j$, it is sufficient to cover the entire space $\mathcal{P}$ with regions $\mathcal{P}_j$ to ensure $g(\mathbf{p}) \leq g^\star$, $\forall \mathbf{p} \in \mathcal{P}$. The geometric parameters for the deployment of the anchors were obtained using Algorithm 1.

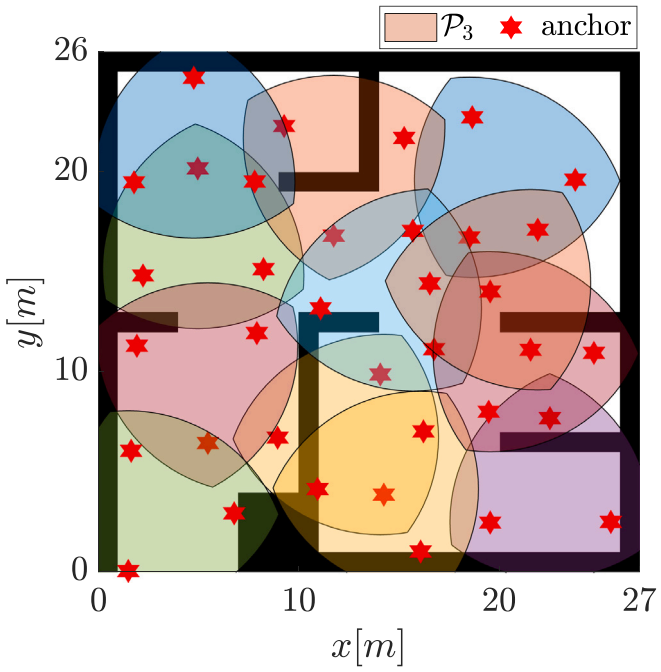


**Fig. 9.** The final deployed anchors for the $\mathcal{P}_3$ cells.

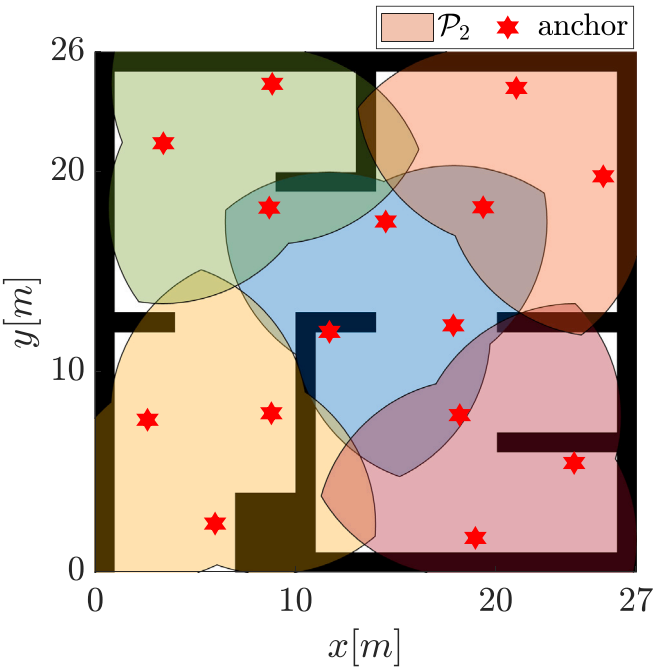


**Fig. 10.** The final deployed anchors for the $\mathcal{P}_2$ cells.

### 5.1. Ranging anchors deployment

The anchor deployment problem as defined here with geometric cells (be them $\mathcal{P}_2$ or $\mathcal{P}_3$) is a special case of the general class of covering problems [21,31,32], where a space $\mathcal{P}$ is fully covered with cells (or tiles) of a given geometry. As shown in [33], the optimal covering of a plane with convex polygons is an NP-Complete problem. Unfortunately, this negative result is obviously applicable to the cell geometry considered in this paper.

However, the coverage problem considered in this paper can be approached adapting the solutions proposed in the literature. For example, a basic solution for NP-Complete covering problems (e.g., vertex cover, hitting set, general set cover, geometric set cover, etc.) is the greedy heuristic vertex covering algorithm proposed by Hochbaum et al. [34]. This approach produces an upper bound for the number of tiles (and hence of anchors) needed for the coverage and has a logarithmic approximation ratio [35]. As discussed next, the covering greedy algorithm in general produces a solution that is not in practice too far from the optimal.

In our example, an initial set of 6000 random cells in equilateral triangle patterns was generated uniformly inside the region of interest. By using the greedy approximation algorithm with $\mathcal{P}_3$ cells, the result is 12 cells deployed with a maximum coverage area of 529 $m^2$ and with a total computation time of 682.5 s. On the other hand, by using $\mathcal{P}_2$ cells, the coverage area was larger, i.e., 552 $m^2$, while the computation time was smaller (416 s) and the algorithm used significantly less cells than in the case of $\mathcal{P}_3$, i.e., just 5. These results were obtained in MathWorks Matlab R2022b software running in Microsoft Windows 10, and using a 2.60 GHz Intel(R) Core(TM) i7 microprocessor endowed with 16 GB RAM. The two deployment are reported in Figs. 9 and 10, respectively. By looking at the deployment results, it appears that the final solution does not provide a full coverage for the map. This is a common problem when heuristic solutions are applied to complex environments. Leaving some parts of the map uncovered is often preferable over using an unnecessarily large number of anchors. However, this problem is solved by placing anchors strictly were needed at the end of the algorithm.

### 5.2. Positioning results

The previous section clearly shows evident advantages in the covering performance of using $\mathcal{P}_2$ over $\mathcal{P}_3$. Our goal is now to show the performance of the two tiles in terms of positioning uncertainty. For this test, we assumed that the ranging uncertainty $\eta_i$ in (2) was the same for all anchors and was distributed according to a Gaussian, white, zero-mean stochastic process with a standard deviation of $\sigma_\ell$. The cell geometry for $\mathcal{P}_2$ and $\mathcal{P}_3$ considered for this test are the one shown in Fig. 11. For all the tests, we assumed a fixed sensing range of $r = 10$ m was used. For $\mathcal{P}_2$, the position estimates are found using the algorithm described in Section 4.2 and the NWLS described in (3)–(5). The corresponding solution for the $\mathcal{P}_3$ is given by the GWLS method [25], which is hence adopted. Notice that, as reported in [25], this will ensure the attainment of the CRLB: to further verify this fact, we also reports the solution for $\mathcal{P}_3$ when the simple Least Squares (LS) is adopted.

For each position in the grid cell, we collected the position estimation error for $m = 1000$ Monte Carlo (MC) simulations. This procedure was repeated with three different measurement standard uncertainties, namely $\sigma_\ell = [0.05, 0.1, 0.2]$ m. The results are reported in Fig. 12 for all the estimation algorithms described above. For the positioning estimation uncertainty, the quantitative results in terms of the Root Mean Square Error (RMSE) were used, i.e.

$$\mathrm{RMSE}_{\mathbf{p}} = \sqrt{\frac{1}{mN}\sum_{i=1}^{N}\sum_{j=1}^{m}\frac{(x_i-\hat{x}_{i,j})^2+(y_i-\hat{y}_{i,j})^2}{2}}$$

where $N$ is the number of grid points in the grid cell, $\mathbf{p}_i = [x_i, y_i]^T$ are the $i$th actual coordinates of the grid cell and $\hat{p}_{i,j} = [\hat{x}_{i,j}, \hat{y}_{i,j}]^T$ are the corresponding estimated coordinates of the $i$th grid cell point for the $j$th MC simulation. The results of Fig. 12 shows that the GWLS surely provides results that are better than LS for the $\mathcal{P}_3$ regardless of the distances $d$ among the anchors and in all the locations on the plane that are covered by the three anchors (see Fig. 11-c). We additionally report with a solid line in Fig. 12 the RMSE for all the points in $\mathcal{P}_2$ (say $\mathrm{RMSE}_2$) when the distance $d_2 = r = 10$ m (grid of Fig. 11-a), used as comparison. This RMSE reports the error between the true target

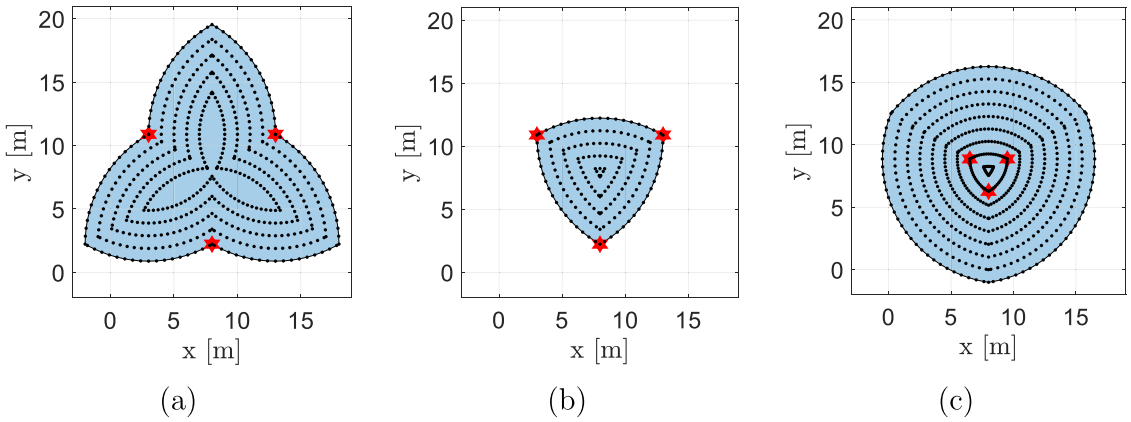


**Fig. 11.** Three sample grid cells with $r = 10$ [m]. (a) $\mathcal{P}_2$ with $d = r$, (b) $\mathcal{P}_3$ with $d = r$, and (c) $\mathcal{P}_3$ with $d = 0.3r$.

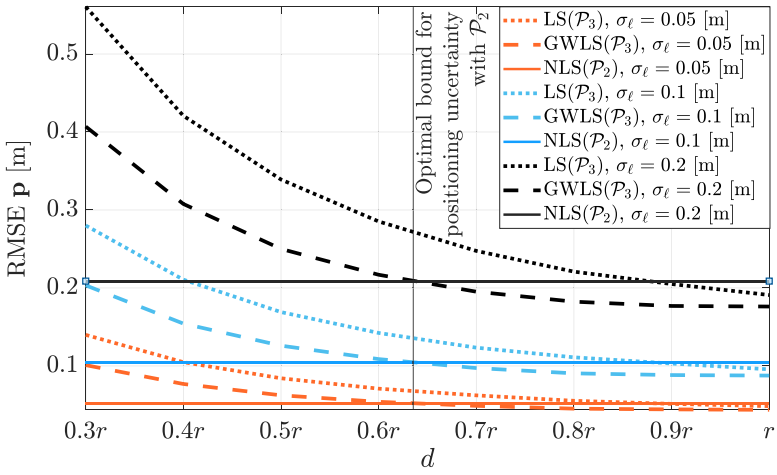


**Fig. 12.** RMSE vs. $d$ for the $\mathcal{P}_2$ and the along the grid points of Fig. 11, for the different estimation algorithms employed and with different distances between the anchors for $\mathcal{P}_3$.

position and the estimated value using NLS, i.e., the intersection point of two ranging measurements in $\mathcal{P}_2$ described in Section 4.2. We then notice that when $d \geq \gamma d_2 = 6.36$ m, (vertical line in Fig. 12) the RMSE for all the points in the region $\mathcal{P}_3$ (say $\text{RMSE}_3$) is smaller than $\text{RMSE}_2$. However, from Theorem 1, we know that there exists a value of $\beta \geq 1.7$ such that for $d_2 = \beta d$ we have that $\mathcal{A}_2 \geq \mathcal{A}_3$ with the same maximum GDoP. Therefore, we have that if $1 < \beta < 1/\gamma = 1.57$, then the $\text{RMSE}_3 < \text{RMSE}_2$, while if $1/\gamma \leq \beta \leq 1.7$, then $\text{RMSE}_3 \geq \text{RMSE}_2$, which is our "approximate optimal bound for positioning uncertainty" for $\mathcal{P}_2$.

## 6. Experimental results

The arena considered for the experiment is the IoT laboratory of the Department of Information Engineering and Computer Science (DISI), University of Trento, a $6 \times 6$ m$^2$ area instrumented with an OptiTrack system equipped with 14 cameras that provides the ground truth data (i.e., the precise location of the anchors in this experiment). We adopted as ranging sensors anchors based on radio frequency technology, namely UWB nodes.

Hence, the target and the testing area are instrumented with DecaWave UWB transceivers (see Fig. 13) with DWM1001 module, which includes a DWM1000 UWB transceiver (compliant with the IEEE802.15.4 UWB physical layer), a Nordic Semiconductor nRF52832 micro-controller unit (MCU) with Bluetooth low Energy (BLE) support, and a three-axis accelerometer. The module operates on 6 frequency bands with base frequencies ranging from 3.5 to 6.5 GHz and a bandwidth of 500 or 900 MHz working with a two-way-ranging-TOA (TWR-TOA) protocol for an asynchronous communication. In addition to the anchors of the infrastructure, the setup comprises one tag as the target, whose position is to be estimated and linked to a laptop, and one anchor configured as initiator to configure the DRTLS network. To prevent interference, a channel access time division multiple access (TDMA) is used to enforce collision-free signal broadcasting from different anchors. In agreement with the IEEE802.15.4 standard, the initiator starts the TDMA cycle for a TWR communication and keeps the clocks of the anchors synchronised. The tag communicates with each anchor within a 25 ms time interval that results in a positioning network system with 10 Hz sampling rate (i.e., one 25 ms slot is allotted to the Initiator) for the total communications and measurements of the whole positioning network system.

The UWB measurement results were collected using three anchors precisely located in an equilateral triangular pattern using the OptiTrack system (having an expanded uncertainty of 1 mm) and placed at 1683 mm off the floor (see Fig. 13). The anchors are placed under line-of-sight (LOS) conditions. However, to ensure realistic environmental conditions, the lab was fully furnished and equipped with several laboratory instruments. The inevitable reflections by the walls, ceiling and different furniture, majorly made of metal in the lab, caused undesired signal interference and attenuation, resulting in biases in the signal time of arrival. This phenomenon is depicted in the two sample measurement error probability mass functions (pmf) obtained from two different UWB anchors and in two different locations on the experimental environment and depicted in Fig. 14. Considering a Type A analysis, we collected ranging measurements at the maximum positioning frequency, i.e. 40 Hz per anchor. The pmfs represent the ranging measurement errors: they were computed by subtracting the

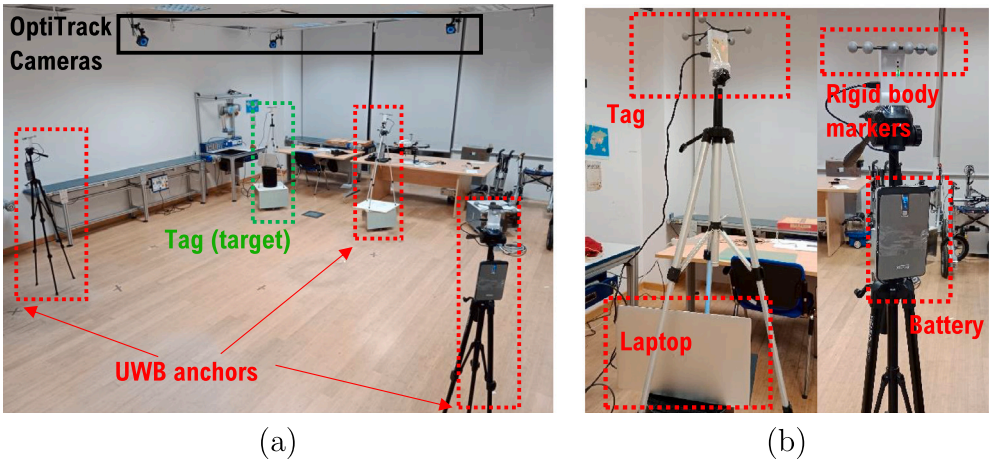


**Fig. 13.** Experimental setup with DecaWave MDEK UWB positioning system. (a) The overview of the arena, and (b) the experimental setup.

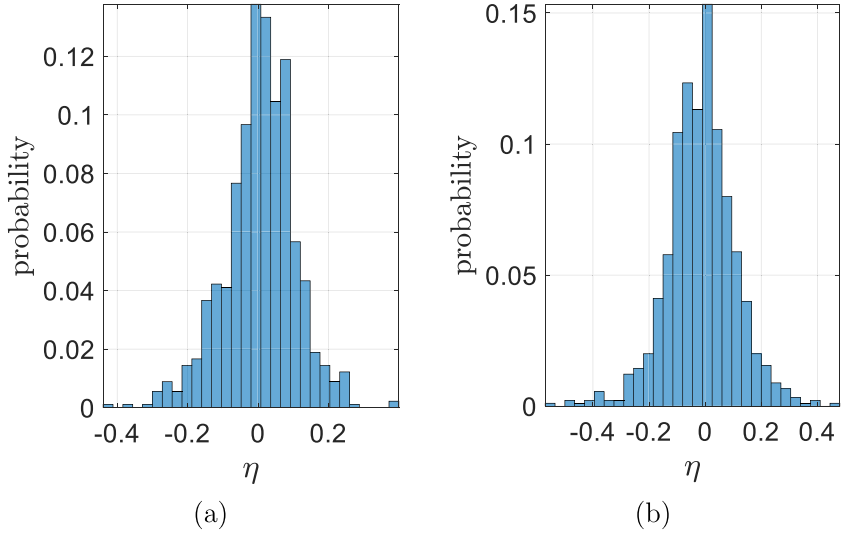


**Fig. 14.** Two sample measurement error pmfs obtained from two different UWB anchors and in two different locations on the experimental environment, with (a) positive and (b) negative bias.

actual distance (i.e., the ground truth distance from stationary target to the UWB anchors retrieved from the OptiTrack system with millimetre accuracy) from the 900 measurement results received from the UWB anchor. From the analysis carried out from two different anchor locations, we observed that the UWB measurements are superimposed with an uncertainty that has standard deviation of $\sigma_\ell = 0.1$ m and a positive/negative maximum bias ranging in the set $\pm 0.28$ cm. The experiment consists of two different equilateral triangular deployment with four sampled locations, all depicted in Fig. 15. In the first scenario, Fig. 15-a, the anchors were located with the same distance $d = 2.59$ m for $\mathcal{P}_2$ and $\mathcal{P}_3$. In the second scenario, the distances between the anchors in $\mathcal{P}_2$ was extended by choosing $\beta = 1.62$, a value close to the optimal bound which was empirically obtained in Section 5 and that has a minimal increase in the covered area but a large average reduction of GDoP. For each position on the map, 900 estimates were made for $\mathcal{P}_2$ and $\mathcal{P}_3$. The GDoP (calculated by the ground truth measurements retrieved by the OptiTrack system) and RMSE results (computed as in Section 5) are reported in Tables 1 and 2, respectively. From Table 2 we can observe how the GDoP in the same exact locations decreases when the distance among the anchors increases. Moreover, when the distance is the same, $\mathcal{P}_2$ conveys a GDoP that is greater than $\mathcal{P}_3$, thus verifying that $\beta > 1$ in light of Theorem 1. Moreover, when $\beta$ increases, we can observe a reduction of the GDoP $\mathcal{P}_2$, but at the price of a reduced area covered $\mathcal{A}_2$ (see Fig. 15). From Table 1, we can notice that with the adopted $\beta = 1.62$, we have a smaller average positioning error for $\mathcal{P}_2$ with respect to $\mathcal{P}_3$, while still preserving a larger coverage area (see Fig. 15-b), which is in perfect accordance with the numerical analysis of Section 5. Finally, from both the tables, we can notice that the RMSE and the GDoP follow the same exact patterns, i.e., when the GDoP of $\mathcal{P}_2$ is less than $\mathcal{P}_3$ so does the RMSE, and vice-versa, which empirically validates once our choice of choosing the GDoP to meet the target uncertainty.

**Table 1**
RMSE values for the four different positions and the two configurations of Fig. 15 with the algorithms described in Section 5.

| Target | $\mathcal{P}_3$(LS) | $\mathcal{P}_3$(GWLS) | $\mathcal{P}_2$ ($d = 2.59$) [m] | $\mathcal{P}_2$ ($d = 4.20$) [m] |
|---|---|---|---|---|
| 1 | 0.179 | 0.123 | 0.145 | 0.096 |
| 2 | 0.179 | 0.111 | 0.133 | 0.095 |
| 3 | 0.218 | 0.143 | 0.150 | 0.111 |
| 4 | 0.090 | 0.076 | 0.15 | 0.096 |

## 7. Conclusion

In this paper, we have presented a novel solution for an algorithm that produces a large scale deployment for ranging sensors so that a

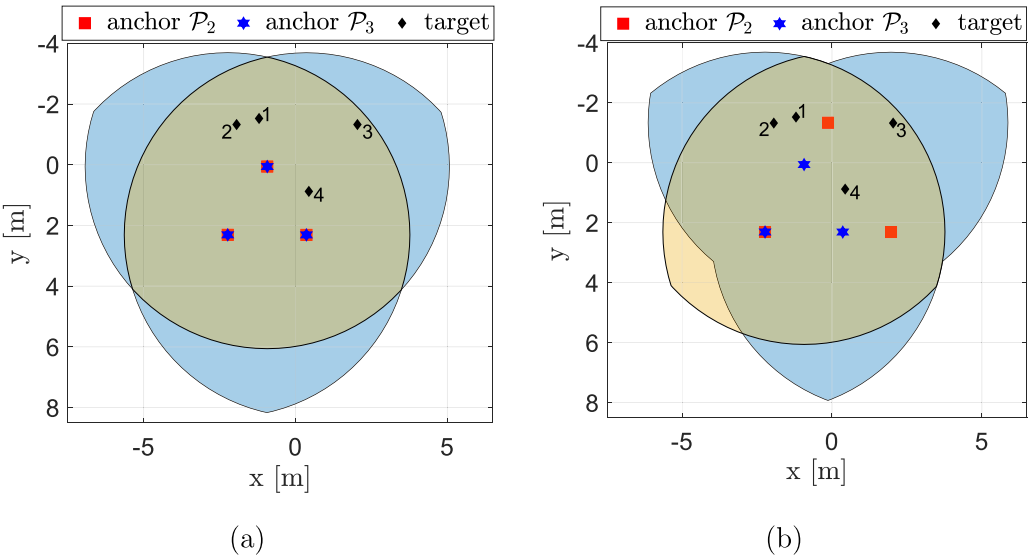


**Fig. 15.** Experimental positioning locations (numbered 1 to 4) and two different anchor deployments. (a) $\mathcal{P}_2$ and $\mathcal{P}_3$ with the same $d = 2.59$ m (b) $\mathcal{P}_2$ with $d = 4.20$ m and $\mathcal{P}_3$ with $d = 2.59$ m.

**Table 2**
GDoP values for the four different positions and the two configurations of Fig. 15.

| Target | $\mathcal{P}_3$ | $\mathcal{P}_2$ ($d = 2.59$) [m] | $\mathcal{P}_2$ ($d = 4.20$) [m] |
|---|---|---|---|
| 1 | 2.260 | 2.338 | 1.419 |
| 2 | 1.947 | 2.168 | 1.419 |
| 3 | 2.126 | 2.190 | 1.414 |
| 4 | 1.454 | 1.596 | 1.455 |

few important requirements are respected. The requirements are of theoretical nature and practical nature and include scalability, generality, optimality, reliability and ability to deal with the physical limitations of the sensors (first and foremost the limited sensing range). We have proposed a two step algorithm in which first a basic cell structure (or tile) is designed and optimised to cover a specified area with guaranteed compliance with the desired target uncertainty, and then this structure is replicated in order to cover the entire space. The key contributions of the paper have been to show: the geometric properties of the cell, an algorithm to design it with a minimal symmetric configuration of anchors, and how the covering efficiency can be maximised when the number of anchors is chosen as the smallest (i.e., $n = 3$).

A large amount of work is still ongoing or is reserved for future investigations. One issue we are coping with is the extension of the proposed analysis with heterogeneous sensing range and to the three/dimensional case. Another direction of work is to study how the proposed results extend to localisation problems and how the cells may be modified still verifying the target uncertainty (this is relevant to adapt the cells to challenging scenarios). In particular, the exploitation of the massive computing power available in the new generation of High Performance Computers will be key to the scalability of the approach. We will study how to define the cell structure to fit the computation style induced by this type of architectures. Moreover, we plan to extend the analysis to more complicated uncertainty models that consider the effect of the environment generating multipath and biases, considering both model-based and data-driven approaches as [36,37] and powerful computing platforms.

## CRediT authorship contribution statement

**Farhad Shamsfakhr:** Conceptualization, Methodology, Investigation, Software, Data curation, Writing – original draft, Validation. **Luigi Palopoli:** Supervision, Investigation, Methodology, Writing – review & editing. **Daniele Fontanelli:** Conceptualization, Supervision, Investigation, Methodology, Writing – original draft, Writing – review & editing.

## Declaration of competing interest

The authors declare that they have no known competing financial interests or personal relationships that could have appeared to influence the work reported in this paper.

## Data availability

No data was used for the research described in the article.

## References

[1] D. Fontanelli, Perception for autonomous systems: A measurement perspective on localisation and positioning, IEEE Instrum. Meas. Mag. 25 (4) (2022) 4–9, http://dx.doi.org/10.1109/MIM.2022.9777773.
[2] A. Filgueira, H. González-Jorge, S. Lagüela, L. Díaz-Vilariño, P. Arias, Quantifying the influence of rain in LiDAR performance, Measurement 95 (2017) 143–148.
[3] N. Ahmed, S.S. Kanhere, S. Jha, On the importance of link characterization for aerial wireless sensor networks, IEEE Commun. Mag. 54 (5) (2016) 52–57.
[4] G. Bellusci, G.J.M. Janssen, J. Yan, C.C.J.M. Tiberius, Model of distance and bandwidth dependency of TOA-based UWB ranging error, in: IEEE International Conference on Ultra-Wideband, Vol. 3, 2008, pp. 193–196, http://dx.doi.org/10.1109/ICUWB.2008.4653448.
[5] N.A. Alsindi, B. Alavi, K. Pahlavan, Measurement and modeling of ultrawideband TOA-based ranging in indoor multipath environments, IEEE Trans. Veh. Technol. 58 (3) (2009) 1046–1058, http://dx.doi.org/10.1109/TVT.2008.926071.
[6] V. Magnago, L. Palopoli, R. Passerone, D. Fontanelli, D. Macii, Effective landmark placement for robot indoor localization with position uncertainty constraints, IEEE Trans. Instrum. Meas. 68 (11) (2019) 4443–4455, http://dx.doi.org/10.1109/TIM.2018.2887071.
[7] P. Nazemzadeh, D. Fontanelli, D. Macii, Optimal placement of landmarks for indoor localization using sensors with a limited range, in: International Conference on Indoor Positioning and Indoor Navigation, IPIN, IEEE, Madrid, Spain, 2016, pp. 1–8, http://dx.doi.org/10.1109/IPIN.2016.7743631.
[8] A.E. Redondi, E. Amaldi, Optimizing the placement of anchor nodes in rss-based indoor localization systems, in: 2013 12th Annual Mediterranean Ad Hoc Networking Workshop (MED-HOC-NET), IEEE, 2013, pp. 8–13.
[9] J.N. Ash, R.L. Moses, On optimal anchor node placement in sensor localization by optimization of subspace principal angles, in: 2008 IEEE International Conference on Acoustics, Speech and Signal Processing, IEEE, 2008, pp. 2289–2292.
[10] B. Tatham, T. Kunz, Anchor node placement for localization in wireless sensor networks, in: 2011 IEEE 7th International Conference on Wireless and Mobile Computing, Networking and Communications (WiMob), IEEE, 2011, pp. 180–187.

[11] S.P. Chepuri, G. Leus, A.-J. van der Veen, Sparsity-exploiting anchor placement for localization in sensor networks, in: 21st European Signal Processing Conference (EUSIPCO 2013), IEEE, 2013, pp. 1–5.
[12] H. Sun, O. Büyüköztürk, Optimal sensor placement in structural health monitoring using discrete optimization, Smart Mater. Struct. 24 (12) (2015) 125034.
[13] K.-V. Yuen, X.-H. Hao, S.-C. Kuok, Robust sensor placement for structural identification, Struct. Control Health Monit. 29 (1) (2022) e2861.
[14] H. Wang, K. Yao, G. Pottie, D. Estrin, Entropy-based sensor selection heuristic for target localization, in: Proceedings of the 3rd International Symposium on Information Processing in Sensor Networks, 2004, pp. 36–45.
[15] C. Papadimitriou, J.L. Beck, S.-K. Au, Entropy-based optimal sensor location for structural model updating, J. Vib. Control 6 (5) (2000) 781–800.
[16] K.-V. Yuen, S.-C. Kuok, Efficient bayesian sensor placement algorithm for structural identification: a general approach for multi-type sensory systems, Earthq. Eng. Struct. Dyn. 44 (5) (2015) 757–774.
[17] S.P. Chepuri, G. Leus, Continuous sensor placement, IEEE Signal Process. Lett. 22 (5) (2014) 544–548.
[18] A. Krause, A. Singh, C. Guestrin, Near-optimal sensor placements in gaussian processes: Theory, efficient algorithms and empirical studies, J. Mach. Learn. Res. 9 (Feb) (2008) 235–284.
[19] S. Liu, E. Masazade, M. Fardad, P.K. Varshney, Sparsity-aware field estimation via ordinary kriging, in: 2014 IEEE International Conference on Acoustics, Speech and Signal Processing, ICASSP, IEEE, 2014, pp. 3948–3952.
[20] Y. Chen, J.-A. Francisco, W. Trappe, R.P. Martin, A practical approach to landmark deployment for indoor localization, in: 2006 3rd Annual IEEE Communications Society on Sensor and Ad Hoc Communications and Networks, Vol. 1, IEEE, 2006, pp. 365–373.
[21] J. Liang, M. Liu, X. Kui, A survey of coverage problems in wireless sensor networks, Sens. Transducers 163 (1) (2014) 240.
[22] R. Zekavat, R.M. Buehrer, HandBook of Position Location: Theory, Practice and Advances, Vol. 27, John Wiley & Sons, 2011.
[23] D. Fontanelli, F. Shamsfakhr, D. Macii, L. Palopoli, An uncertainty-driven and observability-based state estimator for nonholonomic robots, IEEE Trans. Instrum. Meas. 70 (2021) 1–12, http://dx.doi.org/10.1109/TIM.2021.3053066, available online.
[24] F. Shamsfakhr, A. Antonucci, L. Palopoli, D. Macii, D. Fontanelli, Indoor localisation uncertainty control based on wireless ranging for robots path planning, IEEE Trans. Instrum. Meas. 71 (2022) 1–11, http://dx.doi.org/10.1109/TIM.2022.3147316.
[25] D. Fontanelli, F. Shamsfakhr, L. Palopoli, Cramer–rao lower bound attainment in range-only positioning using geometry: The G-WLS, IEEE Trans. Instrum. Meas. 70 (2021) 1–14, http://dx.doi.org/10.1109/TIM.2021.3122521.
[26] I. Sharp, K. Yu, Y.J. Guo, Gdop analysis for positioning system design, IEEE Trans. Veh. Technol. 58 (7) (2009) 3371–3382, http://dx.doi.org/10.1109/TVT.2009.2017270.
[27] S.M. Kay, Fundamentals of Statistical Signal Processing, Prentice Hall PTR, 1993.
[28] C. Wu, W. Su, Y. Ho, A study on gps gdop approximation using support-vector machines, IEEE Trans. Instrum. Meas. 60 (1) (2011) 137–145, http://dx.doi.org/10.1109/TIM.2010.2049228.
[29] R.J. Milliken, C.J. Zoller, Principle of operation of navstar and system characteristics, Navigation 25 (2) (1978) 95–106.
[30] M.P. Fewell, Area of Common Overlap of Three Circles, Tech. rep., Defence Science and Technology Organisation Edinburgh (Australia) Maritime, 2006.
[31] Y.-C. Wang, C.-C. Hu, Y.-C. Tseng, Efficient placement and dispatch of sensors in a wireless sensor network, IEEE Trans. Mob. Comput. 7 (2) (2007) 262–274.
[32] J. Zhu, B. Wang, The optimal placement pattern for confident information coverage in wireless sensor networks, IEEE Trans. Mob. Comput. 15 (4) (2015) 1022–1032.
[33] R.J. Fowler, M.S. Paterson, S.L. Tanimoto, Optimal packing and covering in the plane are np-complete, Inform. Process. Lett. 12 (3) (1981) 133–137.
[34] D.S. Hochbaum, Approximation algorithms for the set covering and vertex cover problems, SIAM J. Comput. 11 (3) (1982) 555–556.
[35] T.H. Cormen, C.E. Leiserson, R.L. Rivest, C. Stein, Introduction To Algorithms, MIT Press, 2009.
[36] K. Manohar, B.W. Brunton, J.N. Kutz, S.L. Brunton, Data-driven sparse sensor placement for reconstruction: Demonstrating the benefits of exploiting known patterns, IEEE Control Syst. Mag. 38 (3) (2018) 63–86.
[37] Y. Saito, T. Nonomura, K. Yamada, K. Nakai, T. Nagata, K. Asai, Y. Sasaki, D. Tsubakino, Determinant-based fast greedy sensor selection algorithm, IEEE Access 9 (2021) 68535–68551.